

A comparative study of intervening and associated H I 21-cm absorption profiles in redshifted galaxies

S. J. Curran^{1*}, S. W. Duchesne¹, A. Divoli² and J. R. Allison³

¹*School of Chemical and Physical Sciences, Victoria University of Wellington, PO Box 600, Wellington 6140, New Zealand*

²*Pingar, 55 Anzac Ave, Auckland 1010, New Zealand*

³*CSIRO Astronomy and Space Science, PO Box 76, Epping NSW 1710, Australia*

Accepted —. Received —; in original form —

ABSTRACT

The star-forming reservoir in the distant Universe can be detected through H I 21-cm absorption arising from either cool gas associated with a radio source or from within a galaxy intervening the sight-line to the continuum source. In order to test whether the nature of the absorber can be predicted from the profile shape, we have compiled and analysed all of the known redshifted ($z \geq 0.1$) H I 21-cm absorption profiles. Although between individual spectra there is too much variation to assign a typical spectral profile, we confirm that associated absorption profiles are, on average, wider than their intervening counterparts. It is widely hypothesised that this is due to high velocity nuclear gas feeding the central engine, absent in the more quiescent intervening absorbers. Modelling the column density distribution of the mean associated and intervening spectra, we confirm that the additional low optical depth, wide dispersion component, typical of associated absorbers, arises from gas within the inner parsec. With regard to the potential of predicting the absorber type in the absence of optical spectroscopy, we have implemented machine learning techniques to the 55 associated and 43 intervening spectra, with each of the tested models giving a $\gtrsim 80\%$ accuracy in the prediction of the absorber type. Given the impracticability of follow-up optical spectroscopy of the large number of 21-cm detections expected from the next generation of large radio telescopes, this could provide a powerful new technique with which to determine the nature of the absorbing galaxy.

Key words: galaxies: active – quasars: absorption lines – galaxies: high redshift – galaxies: ISM – radio lines: galaxies – methods: data analysis

1 INTRODUCTION

Cool neutral hydrogen (H I), the raw material for star formation, is traced through the absorption of radio continuum radiation by the atoms undergoing the 21-cm spin-flip transition. The continuum can be intercepted by gas *associated* with the host galaxy of the radio source or within a galaxy *intervening* the line-of-sight to a more distant source.¹ As well as tracing the star formation history of the Universe (e.g. Lagos et al. 2014) back to $z = 0$, observations of H I give insight into the mass assembly and distribution of galaxies (e.g. Rawlings et al. 2004), a means of detecting the Epoch of Re-ionisation (e.g. Carilli et al. 2004), in addition to the potential to

obtain highly accurate measurements of the fundamental constants of nature at large look-back times (e.g. Curran et al. 2004).

The detection of distant galaxies through 21-cm absorption is a science goal of the forthcoming Square Kilometre Array (SKA, Morganti et al. 2015), which, through its large instantaneous bandwidth and large field-of-view, will avoid observational biases introduced by the conventional requirement of an optical redshift to which to tune the receiver:

- For the associated systems, the optical pre-selection biases toward high ultra-violet luminosities in the source rest-frame, which can be sufficient to ionise all of the neutral gas within the host galaxy (Curran & Whiting 2012), causing the observed paucity of associated 21-cm absorption at high redshift (Curran et al. 2008b, 2011b, 2013a,b; Curran et al. 2016; Grasha & Darling 2011; Allison et al. 2012; Geréb et al. 2015; Aditya et al. 2016).

- For the intervening absorbers, pre-selection using optical redshift biases against optically obscured sight-lines (e.g. Ellison et al. 2005), as well as absorbers rich in molecular gas (Curran et al. 2006, 2011a). These are of particular interest since molecular lines provide excellent probes of the physical and chemical conditions of

* Stephen.Curran@vuw.ac.nz

¹ Intervening absorption usually within galaxies which exhibit damped Lyman- α absorption, which occurs in the UV-band and is redshifted into the optical band at $z \gtrsim 1.7$. A damped Lyman- α absorber (DLA) is defined as having a neutral hydrogen column density exceeding $N_{\text{HI}} = 2 \times 10^{20}$ atoms per cm^{-2} and DLAs could account for more than 80 per-cent of the neutral gas content in the Universe (Prochaska et al. 2005).

the gas (e.g. Muller et al. 2013), as well as the potential to obtain accurate measurements of the fundamental constants from a single species (the OH radical), thus eliminating line-of-sight effects which could mimic an apparent change in the constants (Darling 2003).

In order to obtain an unbiased census of the distribution and abundance of the cool neutral gas along each sight-line, it is therefore necessary to dispense with the optical pre-selection of targets which has dominated previous 21-cm absorption searches, in favour of using wide instantaneous bandwidths free of frequency interference (RFI). Coverage of the whole redshift space to $z \sim 1$ is already possible with the Australian Square Kilometre Array Pathfinder (ASKAP, Allison et al. 2016), although dispensing with optical spectroscopy does present an obstacle in determining the nature of the absorber (see Allison et al. 2015).

In both the near-by and redshifted active galaxies, 21-cm absorption profiles are often found to be broad ($\gtrsim 150$ km s $^{-1}$, Conway & Blanco 1995), due either to more than one deep component (Conway & Blanco 1995; Mundell et al. 1995; Carilli et al. 1998; Pihlström et al. 1999; Taylor et al. 1999; van Langevelde et al. 2000; Taylor et al. 2002; Morganti et al. 2005, 2008, 2009) or additional broad, shallow “wings” to either side of the main component (Mirabel 1989; Morganti et al. 2005; Struve & Conway 2010; Salter et al. 2010; Morganti et al. 2011; Allison et al. 2012; Allison et al. 2013). This broadening of the additional shallow component is believed to arise from cold gas in the sub-pc, fast rotating central black hole accretion disk/obscuring torus, invoked by unified schemes of active galactic nuclei (AGN, e.g. Antonucci 1993; Urry & Padovani 1995). The fast rotating/disturbed gas in the narrow-line region can lead to the broadening of the H I profile in AGN (e.g. Holt et al. 2008), whereas its absence in the more quiescent intervening absorbers results in generally narrower and less complex profiles (e.g. Gupta et al. 2009b). In this paper we investigate the potential of using these differences in the associated and intervening profiles to classify the nature of a newly identified absorption in the absence of complementary optical data. Such a method could provide an invaluable tool in forthcoming spectral scans with the next generation of large radio telescopes.

2 DIFFERENCES IN ASSOCIATED AND INTERVENING 21-CM ABSORPTION SPECTRA

2.1 The sample

As mentioned above, the use of optical redshifts can bias against the detection of 21-cm absorption and this, in conjunction with radio flux limits, the narrow bandwidths free of RFI and the limited frequency coverage of current telescopes, means that the detection of 21-cm absorption at $z \geq 0.1$ (look-back times of $\gtrsim 1$ Gyr) is currently relatively rare, limited to 57 associated and 50 intervening cases (Fig. 1). However, we limit our analysis to these redshifts since we are interested in developing a technique to classify absorbers for future redshifted 21-cm surveys. Exclusion of low redshift absorption also has several advantages:

- Minimising contamination of the sample introduced by differences between the near-by and distant absorption profiles. Even if there are no intrinsic evolutionary differences, the inclusion of spatially resolved absorption/emission, giving several sight-lines, is expected to confuse the analysis of the unresolved sources of interest.

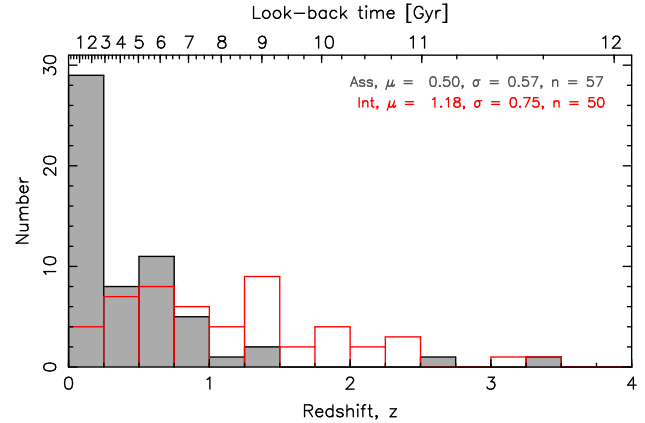


Figure 1. The redshift distribution of detected associated (filled histogram) and intervening (unfilled histogram) $z \geq 0.1$ H I 21-cm absorbers. The mean redshift, μ , and the standard deviation, σ , for each type is shown.

- Dilution of the absorption profile by 21-cm emission, which is very faint beyond these redshifts (e.g. Catinella & Cortese 2015). This effect will be minimal where the spatial resolution is finest, although, again, the mixture of unresolved and resolved features could add confusion.

- Due, at least in part, to the optical pre-selection of 21-cm absorption searches, near-by intervening absorption is limited to 90 sight-lines (see Curran et al. 2016 and reference therein), whereas the near-by associated absorbers have not been compiled. Limiting the analysis to $z \gtrsim 0.1$ ensures approximately equal numbers of associated and intervening absorbers, which is important for class recognition by machine learning models (see Sect. 3.3).

2.2 The spectra

Unlike at lower redshifts, most of the $z \geq 0.1$ detections are already compiled (in Tables 1 & 2, which are updated from Curran & Whiting 2010 and Curran 2010, respectively). However, the raw data were generally unavailable and so the spectra were acquired from the literature by digitising the available figures. For this we used the GETDATA GRAPH DIGITIZER² package for all the spectra, except those in Srianand et al. (2015); Yan et al. (2016), which were constructed from Gaussian parameters presented. This process was successful for 55 associated and 43 intervening spectra, with unsuccessful acquisition resulting from noisy data or low-quality figures. The axes were then normalised by converting the ordinate to observed optical depth (Sect. 2.3) and the abscissa to velocity dispersion, which was defined relative to the optical depth weighted mean velocity of the absorption profile, v_{wm} . For a spectrum sampled over i components this is

$$v_{\text{wm}} = \frac{\sum_i \tau_i v_i}{\sum_i \tau_i}, \quad (1)$$

which is used to shift the abscissa so that $v_{\text{wm}} = 0$.

In order to allow the spectra to be inter-compared and averaged, each was oversampled and then re-binned to a common spectral resolution (see Fig. 2). Since the spectra were shown over a variety of velocity ranges, generally proportional to the line-width, in order to ensure that the full mean velocity range was evenly

² <http://www.getdata-graph-digitizer.com/>

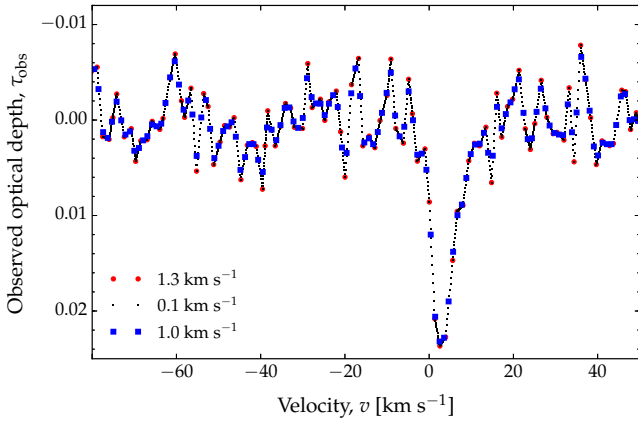


Figure 2. An example of a raw spectrum (with a spectral resolution of 1.3 km s^{-1} , shown as circles) interpolated to 0.1 km s^{-1} (small points) and re-sampled to 1 km s^{-1} (square markers), used for the averaging (Sect. 2.3).

weighted, we added the typical noise level of $\tau_{\text{obs}} \sim 10^{-4}$ to each end of each spectrum to give each the same velocity range.

Half of the original spectra were presented as single or multiple Gaussian fits and so, in order to include these, Gaussian fits were applied to all of the over-sampled spectra. Representing the spectra by Gaussians was also useful in parameterising the spectra for comparison through machine learning (Sect. 3.2.1). Generally, the number of Gaussian components quoted by the authors was used and when this was not given we used the minimum number necessary for a fit. Fitting was done using the FITYK 0.9.8³ package which utilises the Levenberg-Marquardt algorithm, a least-squares fitting routine developed in particular for non-linear fitting.

In Fig. 3 we show the digitised spectra⁴, from which we see a large variation in profile shapes, although the intervening tend to have narrower velocity dispersions. Highlighting this, in Fig. 4 we show the distribution of the effective profile widths of the individual spectra, from which, we see that the associated are, on average, three times wider than the intervening profiles. A Kolmogorov-Smirnov test gives a probability of $P(\text{KS}) = 4.17 \times 10^{-10}$ that the associated and intervening velocity distributions are drawn from the same population, which is significant at $S(\text{KS}) = 6.25\sigma$, assuming Gaussian statistics.

It is therefore clear that the profile width is related to the absorption type: The narrower profile widths of the intervening absorbers being possibly due to the absence of the high dispersion component, in addition to the possibility that intervening absorption may be more favourably detected in galactic disks of high inclination (close to face-on, see Curran et al. 2016). However, the associated absorbers are seen to be roughly equally distributed over the whole range of widths, which makes it difficult to predict the nature of the absorption based upon the FWHM distribution alone.

2.3 Mean spectral properties

Although the profile widths of the individual spectra are too varied to effectively predict the absorber type, we can average the spec-

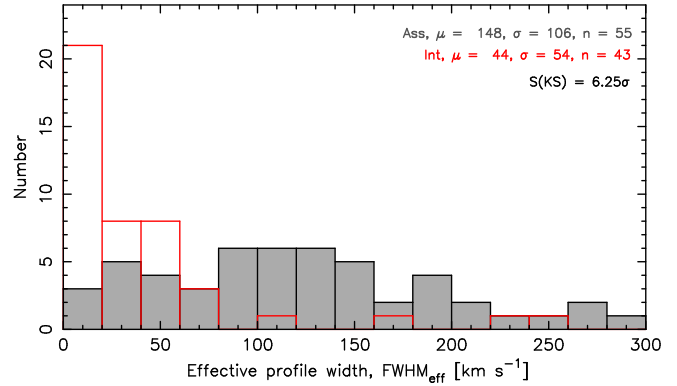


Figure 4. The effective profile width, for the associated (filled histogram) and the intervening (unfilled histogram) absorbers. This is defined by $\text{FWHM}_{\text{eff}} = \int \tau dv / \tau_{\text{peak}}$ (e.g. Dickey 1982; Allison et al. 2013), since for complex profiles (multiple or non-Gaussian), the full-width half maxima are difficult to measure in a consistent manner.

tra in order to explore any strong statistical difference between the types. Since the peak optical depth is not necessarily the centroid of the absorption, we average the spectra by the mean weighted absorption, where the zero velocity offset is defined by the median of the velocity integrated optical depth (Equ. 1), giving a more consistent measure of redshift (e.g. Tzanavaris et al. 2007).

From the mean spectra (shown by the thick traces in Fig. 3), it is clear the associated spectrum has additional low optical depth gas at large velocity dispersions ($|\Delta V| \gtrsim 200 \text{ km s}^{-1}$). As discussed in Sect. 1, it has been hypothesised that this is due to additional fast moving neutral gas close to the nucleus, probably associated with the obscuring torus/accretion disk. In order to model this additional absorption, as a starting point in Fig. 5 (top left) we show the mean profiles, where the blue and redshifted components have been averaged. We then convert each optical depth–dispersion distribution to a column density–radial distribution, by quantifying how the velocity of the gas is expected to vary with galactocentric radius. In Fig. 5 (top right) we fit a polynomial to the velocity distribution of the Milky Way (Bhattacharjee et al. 2014). Being a large spiral this may not represent an accurate depiction of the large-scale rotation curve of an AGN host. However, although early-type galaxies exhibit a variety of rotation curves, many exhibit similar curves to that of the Milky Way (Noordermeer et al. 2007). Furthermore, since we are interested in comparing the associated and intervening absorbers (which themselves may arise in a wide variety of galaxy types, e.g. Wolfe et al. 1986; Matteucci et al. 1997; Prochaska & Wolfe 1997; Haehnelt et al. 1998; Jimenez et al. 1999), the Milky Way provides a classic example of the rapid velocity increase within the central $\lesssim 100 \text{ pc}$, before reaching velocities of $200\text{--}300 \text{ km s}^{-1}$ at $\gtrsim 100 \text{ pc}$ (Noordermeer et al. 2007).

Since the rotation curve of the Milky Way is only well mapped beyond $r \gtrsim 200 \text{ pc}$, we supplement this with data from the Circinus galaxy, a near-by spiral in which the rotation curve at inner radii is readily available. Circinus is known to host a Seyfert 2 nucleus (Moorwood & Oliva 1990; Oliva et al. 1994) and so may at least provide a reasonable model of the inner regions of the associated absorbers. In order to match the velocities between the two galaxies, each of the Circinus values have been upsampled by a factor of 1.7, which is close to the value expected based upon the scaling

³ <http://fityk.nieto.pl/>

⁴ These are presented individually in Duchesne (2015) and machine readable versions of these will be made available in a forthcoming on-line catalogue of the properties of the known redshifted H I 21-cm absorbers.

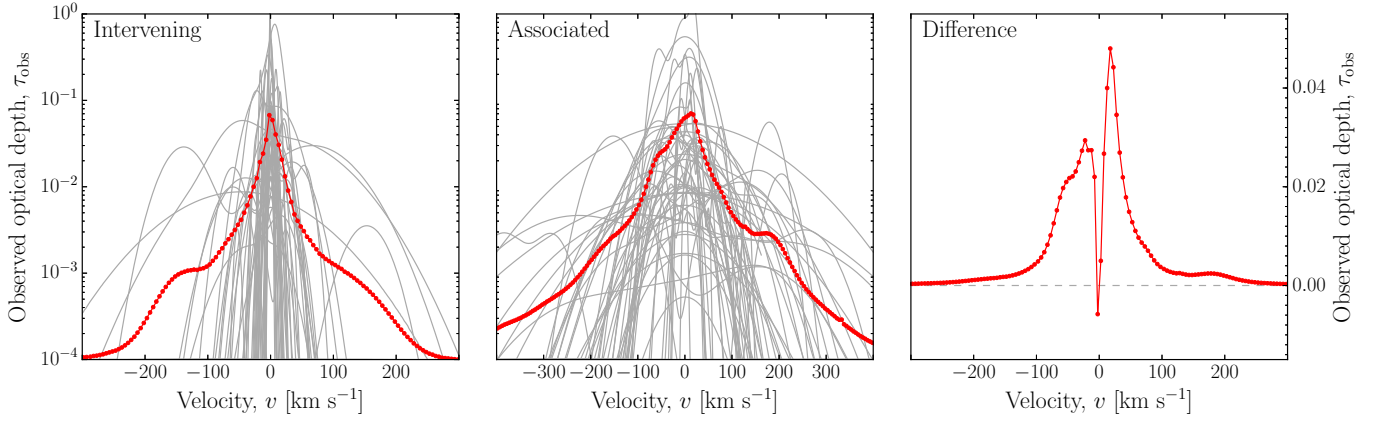


Figure 3. The intervening (left), associated (middle) spectra and the mean associated minus the mean intervening spectrum (right, demonstrating the additional “wings”). The thin traces show the individual spectra and the thick traces the averages of these.

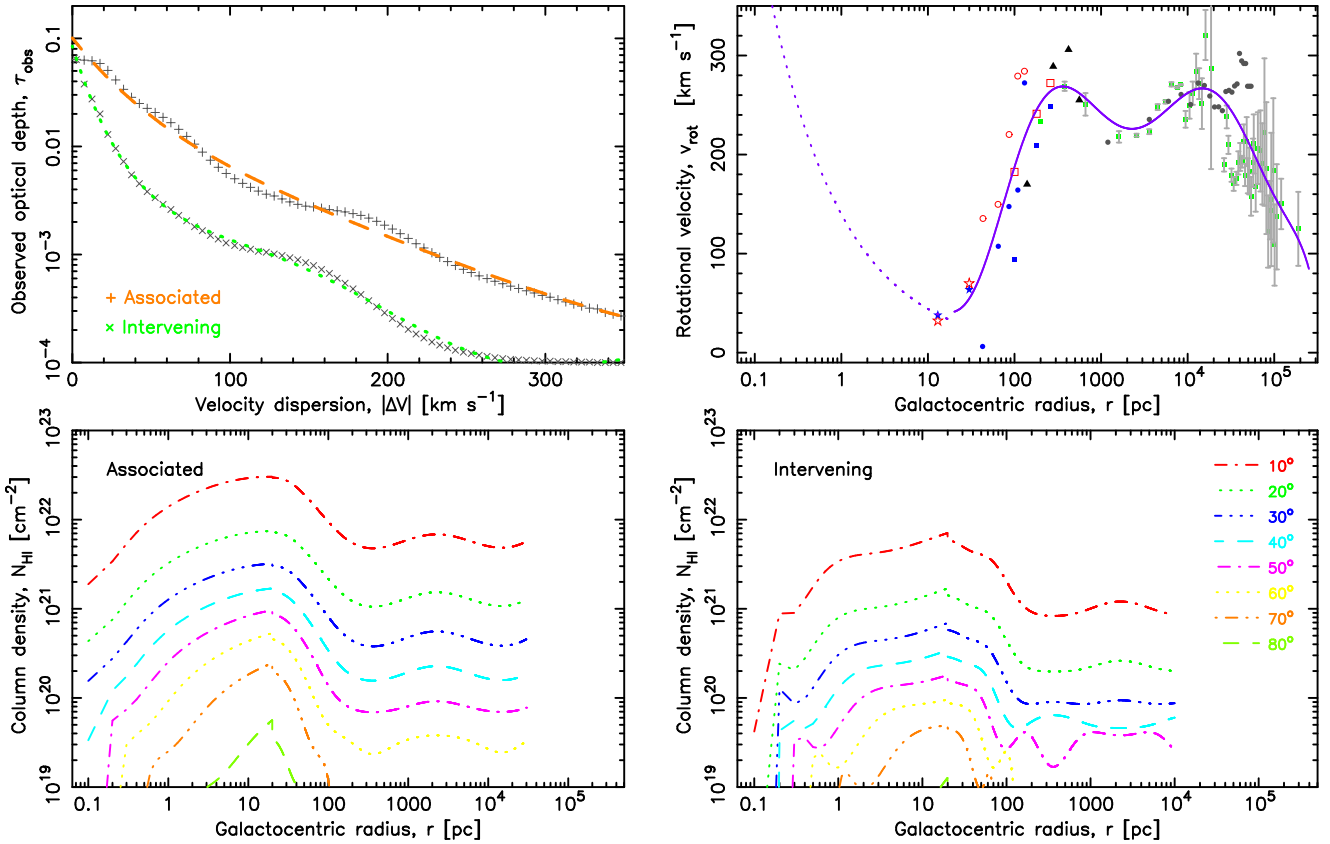


Figure 5. Top left: The mean associated and intervening spectra (where the receding and approaching data are averaged), overlain with low order polynomial fits. Top Right: The rotation curve of a galaxy, based upon data from the Milky Way (shown with error bars, Bhattacharjee et al. 2014) and the Circinus galaxy (compiled from Oliva et al. 1994; Curran et al. 1998; Davies et al. 1998; Maiolino et al. 1998, see Curran et al. 2008a). The full curve shows a polynomial fit to the large-scale Milky Way and Circinus data and the broken curve shows the scaled Keplerian orbit of the H₂O masers within the central 0.4 pc of Circinus (Greenhill et al. 2003), extrapolated to 20 pc to provide continuity. Bottom left: The derived column density distribution at various disk inclinations for the associated absorbers. Bottom right: For the intervening absorbers.

ratio between the nuclear black hole and host galaxy mass (e.g. Ferrarese & Merritt 2000; Bennert et al. 2015).⁵

⁵ For the Milky Way $M_{\text{BH}} \approx 4 \times 10^6 M_{\odot}$ (e.g. Reid & Brunthaler 2004), cf. $1.7 \times 10^6 M_{\odot}$ for Circinus (Greenhill et al. 2003). Assuming circular orbits, this gives $v_{\text{MW}}/v_{\text{Circinus}} \approx \sqrt{4/1.7} \approx 1.5$.

Once the velocity is mapped, the column density is obtained from

$$N_{\text{HI}} = 1.823 \times 10^{18} T_{\text{spin}} \int \tau dv, \quad (2)$$

where T_{spin} is the spin temperature of the gas, which is a measure of the excitation from the lower hyperfine level (Purcell & Field

1956; Field 1959), and $\int \tau dv$ is the velocity integrated optical depth of the absorption. The observed optical depth is related to this via

$$\tau \equiv -\ln\left(1 - \frac{\tau_{\text{obs}}}{f}\right) \approx \frac{\tau_{\text{obs}}}{f}, \text{ for } \tau_{\text{obs}} \equiv \frac{\Delta S}{S_{\text{obs}}} \lesssim 0.3, \quad (3)$$

where the covering factor, f , is a measure of the fraction of observed background flux (S_{obs}) intercepted by the absorber. In the optically thin regime (where $\tau_{\text{obs}} \lesssim 0.3$), Equ. 2 can be rewritten as $N_{\text{HI}} \approx 1.06 \times 1.823 \times 10^{18} (T_{\text{spin}}/f) \tau_{\text{peak}} \Delta V$, where ΔV is the dispersion of the absorption. Assuming that the peak of the absorption occurs, on average, in the centre of the galaxy and that the gas is dynamically coupled to the sub-kpc rotation, the dispersion is related to the rotational velocity via $\Delta V = v_{\text{rot}} \cos i$. To obtain the column density, we assume a constant $T_{\text{spin}} = 500$ K across the disk, since this is a constant 250–400 K across the Milky Way (Dickey et al. 2009) and a constant $T_{\text{spin}}/f \sim 1000$ K ($T_{\text{spin}} \lesssim 1000$ K) across external galaxies (Curran et al. 2016), with a mean of $T_{\text{spin}}/f \approx 2000$ K ($T_{\text{spin}} \lesssim 2000$ K) at higher redshift (in damped Lyman- α absorbers). Higher spin temperatures close the AGN, would lead to higher column densities in the associated absorbers and so those derived (Fig. 5, bottom left) should be considered lower limits. For the covering factor we assume full coverage ($f = 1$) for the mean face-on ($i = 90^\circ$) disk, so that $\tau = \tau_{\text{obs}}/\sin^2 i$ (Curran 2012).

Assuming that the gas remains sufficiently cool and neutral to exhibit detectable 21-cm absorption within the inner ~ 1 pc, where the kinematics are dominated by Keplerian rotation around a massive compact object (the central black hole), this simple model does indeed suggest that additional high dispersion gas in the associated absorbers arises from a central component, rather than being dominated by orientation effects (Sect. 2.1).

Furthermore, the high column densities for the low inclination associated absorbers are consistent with what we expect from the Milky Way, in which the volume density of the neutral gas exhibits an exponential decrease with galactocentric radius according to $n = n_0 e^{-r/R}$, where $n_0 = 13.4 \text{ cm}^{-3}$ and the scale-length $R = 3$ kpc (Kalberla et al. 2007). From $N_{\text{HI}} \equiv \int n dl$, the column density has a maximum at $i = 0^\circ$, given by $N_{\text{HI}} = n_0 \int_0^\infty e^{-r/R} dr = n_0 R = 1.2 \times 10^{23} \text{ cm}^{-2}$, which remains high to large radii, since this is the total volume density integrated over the path length.

2.4 Redshift evolution

In addition to any possible differences in the intervening and associated profiles due to the presence of gas in close proximity to the AGN, it is also possible that differences could be introduced by redshift evolution. Unfortunately, the associated absorbers are predominantly at $z \lesssim 1$, due to higher redshifts preferentially selecting the most UV luminous sources (Sect. 1). For the intervening absorbers, however, the sample is split in half at $z \sim 1$, which, at a look-back time of $\text{LBT} \approx 8$ Gyr, is close to half the age of the Universe, which allows us to compare the profiles between these two epochs.

From the distribution of profile width with redshift (Fig. 6), we see no evidence of any evolution. If the thermal broadening is comparable to that introduced by the gas kinematics (Sect. 2.3), this would suggest no mean evolution in the kinetic temperature of the gas, T_{kin} . The intervening absorbers are not subject to the same broadening mechanisms as the associated absorbers, where gas kinematics, turbulence and radiative heating can be significant,

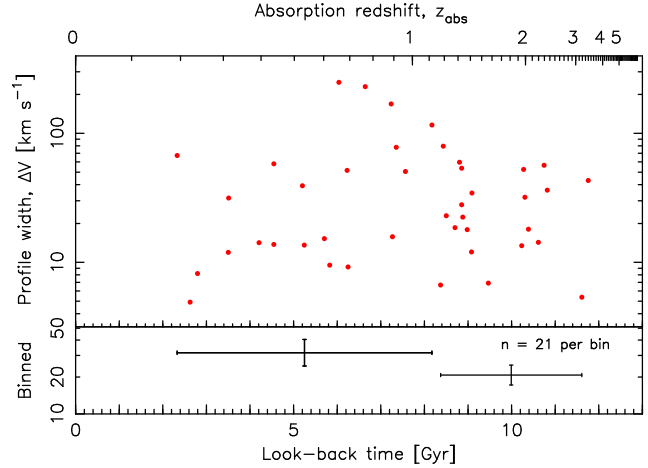


Figure 6. The effective profile width versus look-back time for the intervening absorbers.

leading to possible line broadening (see Fig. 4). That is, in thermodynamic equilibrium the spin temperature is coupled to the kinetic temperature (e.g. Lane & Briggs 2001; Roy et al. 2006), which is given by

$$T_{\text{kin}} \leq \frac{\Delta V^2}{8 \ln(2)} \frac{m_{\text{H}}}{k_{\text{B}}} [\text{K}] \lesssim 22 \Delta V^2 [\text{K for } \Delta V \text{ in km s}^{-1}],$$

where m_{H} is the mass of the hydrogen atom and k_{B} is the Boltzmann constant. From the binned line-widths (Fig. 6), we obtain $T_{\text{kin}} \lesssim 22000$ K at LBTs $\lesssim 8$ Gyr and $T_{\text{kin}} \lesssim 9000$ K at LBTs $\gtrsim 8$ Gyr. The limit arises due to other possible broadening mechanisms, although the absence of any increase in profile width with redshift does not support the argument that there is an increase in temperature with redshift (Kanevar & Chengalur 2003, where the $T_{\text{spin}} = T_{\text{kin}} = 22 \Delta V^2$ assumption is used). This is consistent with the argument that the larger T_{spin}/f ratios measured at high redshift are dominated by lower covering factors (Curran et al. 2005), through the geometry effects of an expanding Universe (Curran 2012).

3 EXPLORING MACHINE LEARNING MODELS FOR CLASSIFICATION

3.1 Motivation for using machine learning

The main motivation for this study was to determine whether the absorber type can be predicted from the profile properties without *a priori* knowledge of the emission redshift from an optical spectrum. As seen in Fig 3, however, the individual spectra are too varied to permit this, with the associated absorbers spanning the full range of line-widths (Fig. 4). We therefore apply machine learning techniques with the aim of building a classifier which can be used to make such a prediction. While the data set is quite limited, with $\lesssim 50$ useful spectra in each class, we can explore how feasible machine learning models are and the potential for prediction, particularly as more data are added. We use the WEKA package (Hall et al. 2009), a suite of machine learning algorithms designed for data mining tasks.

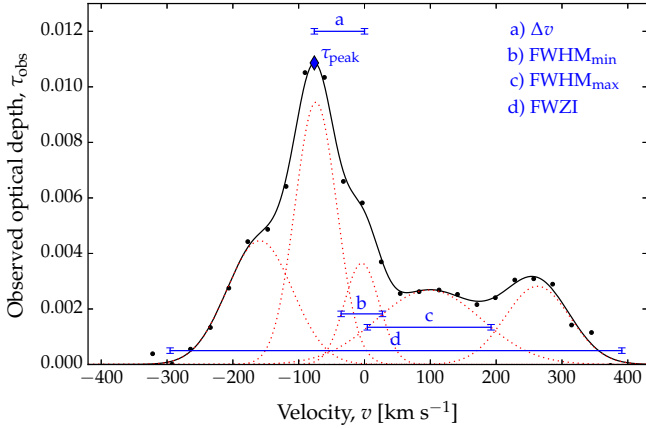


Figure 7. An example of a complex ($n_g = 5$) absorption profile, labelled with the features used for the machine learning: Δv the offset of the component from z_{weight} (a), the minimum (b) and maximum (c) FWHM of the profile and the Full-Width at Zero Intensity (d, where $\tau_{\text{obs}} < 10^{-4}$).

3.2 Models

A model is the result of the training data, the features selected to represent the data, the algorithm used, as well as a number of parameters set for the algorithm.

3.2.1 Feature Selection

A crucial step in machine learning is the selection of *features*. These represent each datum and therefore need to be discriminative and informative. The feature set forms the input given to the selected algorithm and it is the combination of the features which allow different algorithms to discriminate between classes. Here we identified a mixture of such features for each spectrum, illustrated in Fig. 7 and listed in Tables 1 and 2.

Although each spectrum can be quantified through standard parameters such as the number of Gaussians (n_g), the velocity offset (Δv), the peak optical depth (τ_{peak}) and the FWHM, this will present an issue for the machine learning in that for $n_g > 1$ there will be several parameters classified as Δv , τ_{peak} and the FWHM, which must be independently flagged as such while also being compared to other spectra. For example, if both spectra A and B each have two components, then the first component of A, FWHM_1^A , must be compared with both FWHM_1^B and FWHM_2^B , as must FWHM_2^A , while all retaining their identity as representing the line-width of an unspecified component. In machine learning it is common practice to compare global properties, which in this instance would be the total or average FWHM. The chosen features represent unique (or a combination of unique) properties of the spectrum, with no prior expectations of how they will perform. Therefore, in addition to features analogous to those standard in quantifying the spectral properties, such as the line-width and optical depth, we include the average offset of the components from z_{weight} . This is included solely for the reason in that it is an additional property which can be extracted, although there is the possibility that this could be non-zero for the associated spectra, where there is additional in or outflowing gas.

In the final models we excluded z_{weight} itself, although it may be a powerful feature (see Fig. 1), and indeed, upon testing, can increase the precision of the models (see Sect. 3.3). However, we believe that the tendency for the associated absorbers to be detected

Table 3. The rankings of the features for the whole sample and excluding the optically thick absorbers (in descending order for the whole sample).

Feature	Pearson's correlation	
	Whole	Excluding $\tau_{\text{peak}} \geq 0.3$
FWZI	0.5552	0.5423
FWHM max	0.5447	0.5367
FWHM ave	0.5017	0.4943
FWHM min	0.4444	0.4384
τ_{peak} max	0.0907	0.0321
τ_{peak} min	0.0904	0.1580
τ_{peak} ave	0.0782	0.0900
Δv	0.0540	0.0654
n_g	0.0420	0.0494
$\Delta v/\text{FWZI}$	0.0336	0.0648

at $z \lesssim 1$ is due to their optical pre-selection, where at higher redshifts the faint optical light observed is intense ultra-violet in the rest-frame of the source, ionising the gas in the high redshift objects (Curran & Whiting 2012). Since, the SKA and its pathfinders will not be reliant upon optical redshifts, through full redshift spectral scans (Sect. 1), we expect higher redshift detections to be forthcoming giving a z_{weight} distribution more similar to that of the intervening absorbers.

3.2.2 Comparison of predictive power of different features

WEKA also offers the ability to explore the predictive power of the different features via the *Select Attributes* function. This is useful in removing non-contributing features, particularly for large data sets where computational power is an issue. This does not apply to our small sample, although it is of interest to find which features contribute most to the predictive power of the models. In Table 3, we show the rankings returned by the attribute evaluator. From this, we see that all features contribute to the classification. Those related to the profile width contribute the most, while other features make relatively little contribution, including, surprisingly, the number of Gaussians.

3.2.3 Training Data

Since the data set is too small to split into training and testing sets, we use all data, 55 associated and 43 intervening spectra, for training. The models were run for both the whole sample and with the exclusion of spectra exhibiting optically thick components (Equ. 3).

3.2.4 Algorithms

Since there is no single algorithm that is more suited to all cases (e.g. Wopler 1996), nor any previous application of machine learning to 21-cm absorption profiles in the literature, we experimented with different algorithms in WEKA. As this is a small dataset, we kept the default parameters for each algorithm. For the same reason, we considered all features with equal weight. Several algorithms performed comparably well, here we report five of which are classifiers for categorical prediction, as opposed to classifiers for numeric prediction (Witten & Frank 2011):

Table 1. The features of the $z \geq 0.1$ associated 21-cm absorbers. The first column gives the IAU name, followed by the mean-weighted absorption redshift (see Sect. 2.3) and the number of Gaussian components required to fit the spectrum, n_g . The following columns give the Full-Width at Zero Intensity, the peak observed optical depths, the average offset of the components from z_{weight} and the full-width half maxima, respectively (see Fig. 7). The last column gives the reference for the 21-cm absorption.

IAU	z_{weight}	n_g	FWZI	τ_{peak}			$\overline{\Delta v}$		FWHM [km s ⁻¹]			Ref.
				ave	max	min	[km s ⁻¹]	$\overline{\Delta v}/\text{FWZI}$ [km s ⁻¹]	ave	max	min	
B0023-26	0.321409	2	482	0.00573	0.00944	0.00201	-39	-0.081	149	173	126	V03
B0108+388	0.668475	2	426	0.0423	0.0516	0.0329	-5	-0.011	107	139	76	O06
J0141+1353	0.620390	2	92	0.0155	0.0169	0.0141	3	0.031	21	35	8	V03
B0316+16	0.906947	3	243	0.0131	0.0273	0.00226	-7	-0.031	42	95	10	S10
J0410+7656	0.598867	3	785	0.00656	0.0141	0.00268	-154	-0.20	80	104	61	V03
J0414+0534	2.636414	2	575	0.0131	0.0151	0.0111	29	0.051	147	154	141	M99
B0428+20	0.220358	2	951	0.00337	0.00467	0.00207	69	0.073	283	299	268	V03
B0500+019	0.584693	2	224	0.0288	0.036	0.0216	-16	-0.071	54	63	45	C98
B0758+143	1.194147	5	686	0.00461	0.00944	0.00268	25	0.036	112	188	63	I03
J0834+5534	0.240669	1	443	0.00281	0.00281	0.00281	0	—	202	202	202	V03
B0839+458	0.192255	2	325	0.178	0.299	0.0574	-18.4	-0.057	79	84	74	G15
B0859+032	0.288116	2	547	0.0474	0.0560	0.0387	14	0.025	73	92	54	Y16
J0901+2901	0.193870	1	179	0.00053	0.00053	0.00053	0	—	117	117	117	V03
B0902+34	3.396779	1	700	0.00849	0.00849	0.00849	0	—	277	277	277	U91
J0909+4253	0.670341	2	276	0.00647	0.0102	0.00273	55	0.20	61	101	20	V03
B20917+27B	0.206698	2	96	0.0612	0.0819	0.0405	-0.9	-0.0089	230	33	13	Y16
J0942+0623	0.123206	3	191	0.723	0.896	0.381	-13	-0.068	30	45	14	S15
B1003+35	0.099742	3	558	0.0139	0.0203	0.00506	42	0.075	117	203	65	V89
B1107-187	0.491705	2	76	0.0161	0.0189	0.0133	0	0.0046	19	22	17	C11b
J1120+2736	0.111720	1	221	0.159	0.159	0.159	0	—	67	67	67	G15
J1124+1919	0.165161	6	77	0.0407	0.101	0.00549	12	0.15	9	13	7	G06
B1147+557	0.138297	3	234	0.0217	0.0494	0.0204	9	0.038	34	42	22	C11
B1126+569	0.891604	2	464	0.0170	0.0276	0.0063	-25	-0.053	137	170	104	Y16
B1142+052	1.343073	3	157	0.00524	0.00707	0.00352	6	0.037	31	39	15	K09
J1202+1637	0.118568	2	622	0.0213	0.0279	0.0147	6	0.0091	179	231	127	G15
B1203+645	0.371883	1	405	0.00385	0.00385	0.00385	0	—	177	177	177	V03
B1206+469	—	—	—	COULD NOT BE FIT/SPECTRUM OF TOO POOR QUALITY								G15
B1244+49	0.205956	4	686	0.000591	0.000657	0.000463	22	0.032	192	260	119	G15
J1254+1856	—	—	—	COULD NOT BE FIT/SPECTRUM OF TOO POOR QUALITY								G15
J1301+4634	0.205041	3	901	0.00777	0.0108	0.00465	7	0.0081	198	298	111	G15
J1326+3154	0.368430	1	459	0.00170	0.00170	0.00170	0	—	227	227	227	V03
J1347+1217	0.121924	3	336	0.00493	0.0107	0.0018	58	0.150	97	130	23	G06
B1355+441	0.645449	1	1085	0.0537	0.0537	0.0537	0	—	359	359	359	V03
J1357+0046	0.796663	2	295	0.0109	0.013	0.0088	25	0.085	76	80	71	Y16
J1400+6210	0.430137	1	411	0.00611	0.00611	0.00611	0	—	169	169	169	V03
J1409+3604	0.148418	2	249	0.034	0.0373	0.0317	-10	-0.038	57	66	50	C11
B1413+135	0.246079	2	72	0.0288	0.036	0.0216	-16	-0.22	54	63	45	C92
J1422+2105	0.190425	1	544	0.0434	0.0434	0.0434	0	—	183	183	183	G15
B1504+37	0.672634	3	258	0.205	0.335	0.0759	-8	-0.031	45	85	17	C98
B1543+480	1.277005	2	532	0.0425	0.0533	0.0317	-20	-0.038	109	129	89	C13
B1549-79	1.518581	3	330	0.00937	0.0174	0.00439	12	0.035	72	140	34	M01
B1601+5252	0.105545	1	243	0.00974	0.00974	0.00974	0	—	95	95	95	C11
B1603+609	0.559129	1	21	0.0142	0.0142	0.0142	0	—	8	8	8	Y16
B1614+26	0.755466	1	1129	0.0084	0.0084	0.0084	0	—	447	447	447	Y16
B1649-062	0.236387	1	503	0.0238	0.0238	0.0238	0	—	179	179	179	C11c
B1717+547	0.147402	2	351	0.0276	0.0326	0.0225	-7	-0.020	100	149	51	C11
B1814+34	0.243994	1	231	0.0396	0.0396	0.0396	0	—	79	79	79	P00
J1815+6127	0.596812	1	327	0.0207	0.0207	0.0207	0	—	118	118	118	V03
J1821+3942	0.795323	2	259	0.00884	0.01	0.00768	-2	-0.0077	53	61	44	V03
J1944+5448	0.258259	1	795	0.00864	0.00864	0.00864	0	—	313	313	313	V03
J1945+7055	0.100209	1	306	0.55	0.55	0.55	0	—	87	87	87	P99
B2050+36	0.354647	2	109	0.125	0.204	0.0462	-6	-0.055	24	32	16	V03
B2121+248	0.107209	3	527	0.00217	0.00432	0.000999	1	0.002	124	200	70	M89
B2252-089	0.607037	2	286	0.132	0.181	0.0839	0.028 8	—	55	92	18	C11b
J2255+1313	0.543101	1	281	0.00162	0.00162	0.00162	0	—	140	140	140	V03
J2316+0405	0.219135	1	289	0.00305	0.00305	0.00305	0	—	130	130	130	V03
J2355+4950	0.237905	2	272	0.0145	0.0176	0.0114	59	0.22	47	81	13	V03

References: M89 – Mirabel (1989), V89 – van Gorkom et al. (1989), U91 – Uson et al. (1991), C92 – Carilli et al. (1992), C98 – Carilli et al. (1998), M99 – Moore et al. (1999), P99 – Peck et al. (1999), P00 – Peck et al. (2000), M01 – Morganti et al. (2001), I03 – Ishwara-Chandra et al. (2003), V03 – Vermeulen et al. (2003), G06 – Gupta et al. (2006), O06 – Orienti et al. (2006), K09 – Kanekar et al. (2009), S10 – Salter et al. (2010), C11 – Chandra et al. (2011), C11b – Curran et al. (2011b), C11c – Curran et al. (2011c), C13 – Curran et al. (2013b), G15 –

Table 2. As Table 1 but for the $z \geq 0.1$ intervening 21-cm absorbers.

IAU	z_{weight}	n_g	FWZI	τ_{peak}			$\overline{\Delta v}$ [km s ⁻¹]	$\overline{\Delta v}/\text{FWZI}$ [km s ⁻¹]	FWHM [km s ⁻¹]			Ref.
				ave	max	min			ave	max	min	
J0108-0037	1.370985	1	52	0.0731	0.0731	0.0731	0	—	17	17	17	G09b
B0132-097	0.764436	2	519	0.0294	0.0299	0.0288	0	-0.069	110	145	74	K03a
B0201+113	3.386789	2	143	0.0129	0.017	0.0088	-2	-0.015	29	37	22	K14a
B0218+35	0.684651	1	143	0.0454	0.0454	0.0454	0	—	49	49	49	C93
B0235+164	—	—	—	COULD NOT BE FIT/SPECTRUM OF TOO POOR QUALITY								R76
B0237-233	—	—	—	COULD NOT BE FIT/SPECTRUM OF TOO POOR QUALITY								K09
B0248+430	0.394153	3	49	0.175	0.222	0.126	0	0.0041	6	7	4	L01
B0311+430	2.289521	2	145	0.0101	0.0146	0.0055	-14	-0.099	37	40	34	Y07
J0414+0534	0.959790	3	127	0.0113	0.0174	0.00348	13	0.11	26	31	19	C07a
B0438-436	2.347469	2	83	0.00452	0.0059	0.00314	7	0.087	21	24	18	K14a
B0454-234	0.891324	1	39	0.0130	0.0130	0.0130	0	—	15	15	15	G12
B0458-020	1.560516	1	17	0.0233	0.0233	0.0233	0	—	7	7	7	K09
....	2.039484	2	54	0.237	0.334	0.139	4	0.069	12	13	10	K14a
B0738+313	0.220999	2	14	0.0475	0.0634	0.0316	0	0.0071	4	5	3	K01b
J0804+3012	1.190890	2	198	0.00297	0.00392	0.00201	-9	-0.045	66	89	43	G09b
J0808+4950	1.407309	1	28	0.00766	0.00766	0.00766	0	—	11	11	11	G09b
B0809+483	0.436899	2	347	0.0101	0.0167	0.00354	47	0.13	56	72	39	B01
B0827+243	0.524762	1	89	0.00578	0.00578	0.00578	0	—	37	37	37	K01
J0849+5108	0.311991	2	43	0.0415	0.0602	0.0302	-5	-0.11	9	12	5	G13
J0850+5159	1.326818	3	150	0.274	0.441	0.126	-1	-0.0053	28	47	13	G09b
J0852+3435	1.309508	2	193	0.0868	0.0885	0.0851	-8	-0.040	42	62	22	G09b
B0927+469	0.621550	1	22	0.0323	0.0323	0.0323	0	—	9	9	9	Z15
B0952+179	0.237808	1	19	0.013	0.013	0.013	0	—	8	8	8	K01a
B1055+499	1.211757	2	69	0.0121	0.0188	0.00538	-4	-0.059	21	25	16	G09b
B1127-145	0.313012	7	123	0.0522	0.127	0.00327	1	0.0070	111	15	6	C00
B1157+014	1.943628	2	33	0.0564	0.0698	0.0429	2	0.053	8	8	7	K14a
B1229-0207	—	—	—	COULD NOT BE FIT/SPECTRUM OF TOO POOR QUALITY								L01
B1243-072	0.437217	1	39	0.0684	0.0684	0.0684	0	—	13	13	13	L01
B1252+4427	0.911272	3	229	0.0183	0.0277	0.00995	2	0.0083	41	61	27	G12
B1328+307	0.692150	1	8	0.093	0.093	0.093	0	—	9	9	9	D78
B1331+17	—	—	—	COULD NOT BE FIT/SPECTRUM OF TOO POOR QUALITY								B83
J1337+3152	3.17447	1	17	0.611	0.611	0.611	0	—	5	5	5	S12
B1406-076	1.274564	1	71	0.0160	0.0303	0.00601	-1	-0.0089	11	12	10	G12
B1430-178	1.326455	2	119	0.00158	0.00215	0.00101	-6	-0.054	37	57	16	K09
J1431+3952	0.601849	2	39	0.226	0.227	0.224	1	0.026	7	8	6	E12
J1443+0214	0.371540	2	42	0.256	0.402	0.109	0	-0.0060	10	14	6	G13
B1621+047	1.335695	2	65	0.0322	0.0413	0.0231	5	0.068	15	17	12	G09a
B1622+238	0.655943	1	500	0.00877	0.00877	0.00877	0	—	233	233	23	C07b
B1629+120	0.531764	2	44	0.0211	0.0261	0.0161	1	0.027	13	21	6	K03b
B1755+758	1.970875	1	137	0.0227	0.0227	0.0227	0	—	49	49	49	K14b
B1830-21	0.885469	2	574	0.0338	0.0368	0.0307	-18	-0.032	132	197	67	C99
...	0.192504	3	124	0.0116	0.0134	0.00954	2	0.017	24	28	15	L96
B1850+402	1.989599	2	88	0.0784	0.0956	0.0612	5	0.058	18	20	16	K14b
B2003-025	1.410732	2	64	0.00498	0.00587	0.00408	-5	-0.082	18	24	12	K09
B2029+121	1.115735	2	266	0.0156	0.0186	0.0125	-3	-0.012	70	78	61.4	G12
B2039+187	2.191798	1	38	0.0320	0.0320	0.0320	0	—	13	13	13	K12
J2340-0053	1.360890	3	6	0.400	0.82	0.182	0	0.022	3	6	1	G09b
B2351+456	—	—	—	COULD NOT BE FIT/SPECTRUM OF TOO POOR QUALITY								D04
B2355-106	1.173038	1	17	0.0333	0.0333	0.0333	0	—	6	6	6	G09b

References: R76 – Roberts et al. (1976), D78 – Davis & May (1978), B83 – Briggs & Wolfe (1983), C93 – Carilli et al. (1993), L96 – Lovell et al. (1996), C99 – Chengalur et al. (1999), B01 – Briggs et al. (2001), L01 – Lane & Briggs (2001), K01a – Kanekar & Chengalur (2001), K01b – Kanekar et al. (2001), K03a – Kanekar & Briggs (2003), K03b – Kanekar & Chengalur (2003), D04 – Darling et al. (2004), C07a – Curran et al. (2007a), C07b – Curran et al. (2007b), Y07 – York et al. (2007), G09a – Gupta et al. (2009a), G09b – Gupta et al. (2009b), K09 – Kanekar et al. (2009), E12 – Ellison et al. (2012), G12 – Gupta et al. (2012), K12 – Kanekar et al. (2013), S12 – Srianand et al. (2012), G13 – Gupta et al. (2013), K14a – Kanekar et al. (2014), K14b – Kanekar (2014), Z15 – Zwaan et al. (2015).

Table 5. The confusion matrices for the models in Table 4.

	Whole sample	Excluding $\tau_{\text{peak}} \geq 0.3$
Bayesian Network	$\begin{bmatrix} 43 & 12 \\ 7 & 36 \end{bmatrix}$	$\begin{bmatrix} 44 & 8 \\ 7 & 31 \end{bmatrix}$
Sequential Minimal Optimisation	$\begin{bmatrix} 39 & 16 \\ 5 & 38 \end{bmatrix}$	$\begin{bmatrix} 37 & 15 \\ 6 & 32 \end{bmatrix}$
Classification Via Regression	$\begin{bmatrix} 43 & 12 \\ 8 & 35 \end{bmatrix}$	$\begin{bmatrix} 41 & 11 \\ 11 & 27 \end{bmatrix}$
Logistic Model Tree	$\begin{bmatrix} 44 & 11 \\ 8 & 35 \end{bmatrix}$	$\begin{bmatrix} 40 & 12 \\ 8 & 30 \end{bmatrix}$
Random Forest	$\begin{bmatrix} 46 & 9 \\ 9 & 34 \end{bmatrix}$	$\begin{bmatrix} 44 & 8 \\ 9 & 29 \end{bmatrix}$

(i) *Bayesian Network* from the “Bayes” group (Bouckaert 2004). This is a probabilistic model, which through the learning of Bayesian nets, represents a set of random variables which may be observable quantities, latent variables, unknown parameters or hypotheses (Bouckaert 2008).

(ii) *Sequential Minimal Optimisation* from the “functions” group. This algorithm solves the quadratic programming problem, arising from the training of support vector machines (Platt 1999).

(iii) *Classification Via Regression* from the “meta” group. This algorithm uses regression methods, where one regression model is built for each class value (Frank et al. 1998).

(iv) *Logistic Model Tree* from the “trees” group. This combines logistic regression and decision tree learning, based upon an earlier version of the tree. Each “leaf” in the tree represents a model and the logistic variant produces a regression model at every node in the tree, which is then split (Landwehr et al. 2005).

(v) *Random Forest* also from the “trees” group. These are an ensemble of learning methods for classification, which operate via a multitude of decision trees (Breiman 2001).

3.3 Results

We summarise the results in Table 4. We report on 10-fold cross validation performance, where the data is split into 10 sets, each of which will contain $(55 + 43)/10 \approx 10$ spectra. Nine of the datasets are used to train the model, with the resulting classifier used to test the one remaining dataset. This process is randomised and repeated ten times with the mean accuracy being reported. 10-fold cross validation is typical practice for small data sets, where there is not enough data to split for training and testing.

Table 5, shows the confusion matrices associated with the models. These are in the format,

	Predicted Ass	Predicted Int
Actual Associated	TA	FI
Actual Intervening	FA	TI

where TA – true associated, FA – false associated, TI – true intervening, FI – false intervening. For example, for the confusion matrix $\begin{bmatrix} 43 & 12 \\ 7 & 36 \end{bmatrix}$, out of $43 + 12$ associated spectra the model correctly identifies 43 as associated and 12 erroneously as intervening and out of $7 + 36$ intervening spectra, 36 are correctly identified as intervening and 7 erroneously as associated. The data in the confusion matrices form the raw data used for reporting several evaluation measures – the precision, recall, F-measure and accuracy (Table 4). Those in Table 5 show that the two classes are balanced in terms of training and classification. For instance, a

matrix such as $\begin{bmatrix} 90 & 0 \\ 10 & 0 \end{bmatrix}$, would return a 90% accuracy, but in this case the model would have a 100% recognition rate for one class and 0% for the other.

3.4 Discussion

Most of the models return a precision, recall, F-measure and accuracy of $\gtrsim 80\%$, making us optimistic that as more data are collected by the community, machine learning can provide a useful tool for classification of redshifted 21-cm absorption spectra.

During our feature selection experimentation we found that the accuracy of prediction is dominated by the profile width – models trained on the FWZI alone return accuracies just a few percent below those reported in Table 4. Models trained on the three FWHM features give accuracies $\approx 5\%$ lower. The removal of all line-width information features, reduces the accuracy to $\approx 50\%$, i.e. what we would obtain from chance. The number of components, n_g , contributes relatively little to the prediction, which is surprising since we expect the associated profiles to be more complex. However, the combination of all features do provide the better performing models, in agreement with the attribute evaluator analysis (Table 3).

Another feature we considered is z_{weight} . Some experimentation with classifiers trained using the z_{weight} as an additional feature improved the precision in some cases (e.g. up to 5.2%, from 78.5% to 83.7% for the Sequential Minimal Optimisation algorithm, excluding the $\tau_{\text{peak}} \geq 0.3$ set), while being detrimental in others (e.g. Bayesian Network). However, since the purpose of this work is to classify the absorber type without the use of an optical redshift, the pre-selection of which may introduce a bias (Sect. 1), we did not consider z_{weight} in the final models (Table 4).

The machine learning results are very encouraging and, as more data are added, we expect the predictive power of such classifiers to improve. This will prove invaluable as the number of new 21-cm detections becomes too large to feasibly follow-up with optical observations.

4 CONCLUSIONS

Forthcoming spectral lines surveys with the next generation of large radio telescopes are expected to detect large numbers of new redshifted H I 21-cm absorbers. Although the measured redshifts of the absorbing galaxies will be extremely accurate, due to the phase-locking of radio receivers, without follow-up optical band observations it is generally not possible to determine whether the absorption arises within the source host or from a galaxy intervening the sight-line to a more distant radio source. Given these large numbers, and the possibility that optical pre-selection biases against the detection of cool, neutral gas, it would be of great value to be able to determine the nature of the absorber based upon the radio data alone.

To this end, we have compiled and digitised the known $z \gtrsim 0.1$ H I 21-cm absorbers, converted these to consistent dimensions (optical depth and velocity) and re-sampled to a common spectral resolution. However, the normalised spectra in each of the associated and intervening classes exhibit a wide range of profile shapes, not making it possible to manually ascertain a typical profile shape. By applying machine learning algorithms, we find that, even for our limited sample of $\lesssim 50$ of each type of absorber, the type can be predicted with $\gtrsim 80\%$ accuracy. As new detections are made,

Table 4. The models, without the z_{weight} feature, and their performance for the whole sample and excluding the optically thick absorbers. $P = t_p/(t_p + f_p)$ is the precision (the positive predictive value), where t_p is the number of true positives and f_p the number of false positives. $R = t_p/(t_p + f_n)$ is the recall (the fraction of relevant instances that are retrieved), where f_n is the number of false negatives and the F-measure, $F = 2PR/(P + R)$, is the harmonic mean of precision and recall. The accuracy, A , is the fraction of correctly classified instances. The mean absolute error, $|\bar{\sigma}|$, is a measure of how close the predictions are to the eventual outcomes. The κ -statistic is the chance-corrected measure of agreement between the classifications and the true classes – $\kappa > 0$ signifies that the classifier is doing better than predicting by chance and $\kappa = 1$ signifies completely accurate prediction.

Algorithm	P [%]	R [%]	F [%]	A [%]	$ \bar{\sigma} $	κ	P [%]	R [%]	F [%]	A [%]	$ \bar{\sigma} $	κ
	Whole (55 associated/43 intervening)						Excluding $\tau_{\text{peak}} \geq 0.3$ (52 associated/39 intervening)					
Bayesian Network	81.2	80.6	80.7	80.6	0.194	0.611	83.4	83.3	83.4	83.3	0.182	0.660
Sequential Minimal Optimisation	80.6	78.6	78.6	78.6	0.214	0.577	78.5	76.7	76.8	76.9	0.233	0.537
Classification Via Regression	80.0	79.6	79.7	79.6	0.302	0.590	75.6	75.6	75.6	76.9	0.333	0.499
Logistic Model Tree	80.9	80.6	80.7	80.6	0.346	0.610	78.3	77.8	77.9	77.8	0.353	0.551
Random Forest	81.6	81.6	81.6	81.6	0.305	0.422	81.1	81.1	81.1	81.1	0.312	0.612

follow-up optical-band observations will allow us to improve the classifier in preparation for forthcoming H I 21-cm surveys with the SKA and its precursors.

Although machine learning was invoked to classify the individual spectra, by averaging all those in each class in order to examine the bulk differences, we find:

(i) That the mean associated profile is wider than the mean intervening profile, with a Kolmogorov-Smirnov of the individual widths giving a 4×10^{-10} probability that the associated and intervening velocity distributions are drawn from the same population. This is consistent with the profile width being the one single feature which lowers the predictive power of the classifier to that of chance when removed.

(ii) From a simple model of the H I column density distribution, that the high velocity wings often observed in associated absorption, arise from the sub-pc gas, which appears to be absent in the intervening absorbers. This supports the widely proposed conjecture that the additional component of the associated absorption is due to the dense circumnuclear torus, invoked by unified schemes of AGN. This is also consistent with hypothesis that associated absorption arises in AGN (radio galaxies and quasars), where significant amounts of gas are accreted onto the central super-massive black hole, whereas intervening absorption arises in more quiescent galaxies.

(iii) The consistency in the mean intervening profile widths to either side of $z \sim 1$ (where the sample is split in half), indicates no kinematical or thermal evolution with redshift. While the H I column density model is consistent with the bulk of profile broadening being kinematical, rather than thermal, in nature, this result does not support the proposed increase in the spin temperature of the gas with redshift in damped Lyman- α absorbers.

ACKNOWLEDGEMENTS

We wish to thank the anonymous referee for their detailed comments and Nathan Holmberg for his advice. This research has made use of the NASA/IPAC Extragalactic Database (NED) which is operated by the Jet Propulsion Laboratory, California Institute of Technology, under contract with the National Aeronautics and Space Administration and NASA's Astrophysics Data System Bibliographic Service. This research has also made use of NASA's Astrophysics Data System Bibliographic Service.

REFERENCES

- Aditya J. N. H. S., Kanekar N., Kurapati S., 2016, MNRAS, 455, 4000
- Allison J. R. et al., 2012, MNRAS, 423, 2601
- Allison J. R., Curran S. J., Sadler E. M., Reeves S. N., 2013, MNRAS, 430, 157
- Allison J. R. et al., 2016, Astronomische Nachrichten, 337, 175
- Allison J. R. et al., 2015, MNRAS, 453, 1249
- Antonucci R. R. J., 1993, ARA&A, 31, 473
- Bennert V. N. et al., 2015, ApJ, 809, 20
- Bhattacharjee P., Chaudhury S., Kundu S., 2014, ApJ, 785, 63
- Bouckaert R. R., 2004, Bayesian networks in Weka. Tech. rep., University of Waikato
- Bouckaert R. R., 2008, Bayesian Network Classifiers in Weka for Version 3-5-7. Tech. rep., University of Waikato
- Breiman L., 2001, Machine Learning, 45, 5
- Briggs F. H., de Bruyn A. G., Vermeulen R. C., 2001, A&A, 373, 113
- Briggs F. H., Wolfe A. M., 1983, ApJ, 268, 76
- Carilli C. L., Gnedin N., Furlanetto S., Owen F., 2004, Science with the Square Kilometer Array, New Astronomy Reviews 48, Carilli C. L., Rawlings S., eds., Elsevier, Amsterdam, pp. 1053–1061
- Carilli C. L., Menten K. M., Reid M. J., Rupen M. P., Yun M. S., 1998, ApJ, 494, 175
- Carilli C. L., Perlman E. S., Stocke J. T., 1992, ApJ, 400, L13
- Carilli C. L., Rupen M. P., Yanny B., 1993, ApJ, 412, L59
- Catinella B., Cortese L., 2015, MNRAS, 446, 3526
- Chandola Y., Sirothia S. K., Saikia D. J., 2011, MNRAS, 418, 1787
- Chengalur J. N., de Bruyn A. G., Narasimha D., 1999, A&A, 343, L79
- Conway J. E., Blanco P. R., 1995, ApJ, 449, L131
- Curran S. J., 2010, MNRAS, 402, 2657
- Curran S. J., 2012, ApJ, 748, L18
- Curran S. J., Allison J. R., Whiting M. T., Sadler E. M., Combes F., Pracy M. B., Bignell C., Athreya R., 2016, MNRAS, 457, 3666
- Curran S. J., Darling J. K., Bolatto A. D., Whiting M. T., Bignell C., Webb J. K., 2007a, MNRAS, 382, L11
- Curran S. J., Johansson L. E. B., Rydbeck G., Booth R. S., 1998, A&A, 338, 863
- Curran S. J., Kanekar N., Darling J. K., 2004, Science with the Square Kilometer Array, New Astronomy Reviews 48, Carilli

- C. L., Rawlings S., eds., Elsevier, Amsterdam, pp. 1095–1105
- Curran S. J., Koribalski B. S., Bains I., 2008a, *MNRAS*, 389, 63
- Curran S. J., Murphy M. T., Pihlström Y. M., Webb J. K., Purcell C. R., 2005, *MNRAS*, 356, 1509
- Curran S. J., Reeves S. N., Allison R., Sadler E. M., 2016, *MNRAS*, 459, 4136
- Curran S. J., Tzanavaris P., Pihlström Y. M., Webb J. K., 2007b, *MNRAS*, 382, 1331
- Curran S. J., Whiting M. T., 2010, *ApJ*, 712, 303
- Curran S. J., Whiting M. T., 2012, *ApJ*, 759, 117
- Curran S. J. et al., 2011a, *MNRAS*, 416, 2143
- Curran S. J. et al., 2011b, *MNRAS*, 413, 1165
- Curran S. J., Whiting M. T., Murphy M. T., Webb J. K., Longmore S. N., Pihlström Y. M., Athreya R., Blake C., 2006, *MNRAS*, 371, 431
- Curran S. J., Whiting M. T., Sadler E. M., Bignell C., 2013a, *MNRAS*, 428, 2053
- Curran S. J., Whiting M. T., Tanna A., Sadler E. M., Pracy M. B., Athreya R., 2013b, *MNRAS*, 429, 3402
- Curran S. J., Whiting M. T., Webb J. K., Athreya A., 2011c, *MNRAS*, 414, L26
- Curran S. J., Whiting M. T., Wiklind T., Webb J. K., Murphy M. T., Purcell C. R., 2008b, *MNRAS*, 391, 765
- Darling J., Giovanelli R., Haynes M. P., Bower G. C., Bolatto A. D., 2004, *ApJ*, 613, L101
- Darling J. K., 2003, *PhRvL*, 91, 011301
- Davies R. I. et al., 1998, *MNRAS*, 293, 189
- Davis M. M., May L. S., 1978, *ApJ*, 219, 1
- Dickey J. M., 1982, *ApJ*, 263, 87
- Dickey J. M., Strasser S., Gaensler B. M., Haverkorn M., Kavars D., McClure-Griffiths N. M., Stil J., Taylor A. R., 2009, *ApJ*, 693, 1250
- Duchesne S. W., 2015, *Star-Forming Gas in the Distant Universe: Distinguishing between intervening and gas associated with the radio source for the next generation of large radio telescopes*. Tech. rep., Victoria University of Wellington
- Ellison S., Kanekar N., and Prochaska J. X., Momjian E., Worseck G., 2012, *MNRAS*, 424, 293
- Ellison S. L., Hall P. B., Lira P., 2005, *AJ*, 130, 1345
- Ferrarese L., Merritt D., 2000, *ApJ*, 539, L9
- Field G. B., 1959, *ApJ*, 129, 536
- Frank E., Wang Y., Inglis S., Holmes G., Witten I., 1998, *Machine Learning*, 32, 63
- Geréb K., Maccagni F. M., Morganti R., Oosterloo T. A., 2015, *A&A*, 575, 44
- Grasha K., Darling J., 2011, in *American Astronomical Society Meeting Abstracts*, Vol. 43, p. 345.02
- Greenhill L. J. et al., 2003, *ApJ*, 590, 162
- Gupta N., Salter C. J., Saikia D. J., Ghosh T., Jeyakumar S., 2006, *MNRAS*, 373, 972
- Gupta N., Srianand R., Noterdaeme P., Petitjean P., Muzahid S., 2013, *A&A*, 558, A84
- Gupta N., Srianand R., Petitjean P., Bergeron J., Noterdaeme P., Muzahid S., 2012, *A&A*, 544, 21
- Gupta N., Srianand R., Petitjean P., Noterdaeme P., Saikia D. J., 2009a, in *Astronomical Society of the Pacific Conference Series*, Vol. 407, *The Low-Frequency Radio Universe*, Saikia D. J., Green D. A., Gupta Y., Venturi T., eds., p. 67
- Gupta N., Srianand R., Petitjean P., Noterdaeme P., Saikia D. J., 2009b, *MNRAS*, 398, 201
- Haehnelt M. G., Steinmetz M., Rauch M., 1998, *ApJ*, 495, 647
- Hall M., Frank E., Holmes G., Pfahringer B., Reutemann P., Witten I., 2009, *SIGKDD Explorations*, 11, 10
- Holt J., Tadhunter C. N., Morganti R., 2008, *MNRAS*, 387, 639
- Ishwara-Chandra C. H., Dwarakanath K. S., Anantharamaiah K. R., 2003, *JA&A*, 24, 37
- Jimenez R., Bowen D. V., Matteucci F., 1999, *ApJ*, 514, L83
- Kalberla P. M. W., Dedes L., Kerp J., Haud U., 2007, *A&A*, 469, 511
- Kanekar N., 2014, *ApJ*, 797, L20
- Kanekar N., Briggs F. H., 2003, *A&A*, 412, L29
- Kanekar N., Chengalur J. N., 2001, *MNRAS*, 325, 631
- Kanekar N., Chengalur J. N., 2003, *A&A*, 399, 857
- Kanekar N., Ellison S. L., Momjian E., York B. A., Pettini M., 2013, *MNRAS*, 532
- Kanekar N., Ghosh T., Chengalur J. N., 2001, *A&A*, 373, 394
- Kanekar N., Prochaska J. X., Ellison S. L., Chengalur J. N., 2009, *MNRAS*, 396, 385
- Kanekar N. et al., 2014, *MNRAS*, 438, 2131
- Lagos C. D. P., Baugh C. M., Zwaan M. A., Lacey C. G., Gonzalez-Perez V., Power C., Swinbank A. M., van Kampen E., 2014, *MNRAS*, 440, 920
- Landwehr N., Hall M., E. Frank, 2005, *Machine Learning*, 95, 161
- Lane W. M., Briggs F. H., 2001, *ApJ*, 561, L27
- Lovell J. E. J. et al., 1996, *ApJ*, 472, L5
- Maiolino R., Krabbe A., Thatte N., Genzel R., 1998, *ApJ*, 493, 650
- Matteucci F., Molaro P., Vladilo G., 1997, *A&A*, 321, 45
- Mirabel I. F., 1989, *ApJ*, 340, L13
- Moore C. B., Carilli C. L., Menten K. M., 1999, *ApJ*, 510, L87
- Moorwood A. F. M., Oliva E., 1990, *A&A*, 239, 78
- Morganti R., Emonts B., Oosterloo T., 2009, *A&A*, 496, L9
- Morganti R., Holt J., Tadhunter C., Ramos Almeida C., Dicken D., Inskip K., Oosterloo T., Tzioumis T., 2011, *A&A*, 535, A97
- Morganti R., Oosterloo T., Struve C., Saripalli L., 2008, *A&A*, 485, L5
- Morganti R., Oosterloo T. A., Tadhunter C. N., van Moorsel G., Emonts B., 2005, *A&A*, 439, 521
- Morganti R., Oosterloo T. A., Tadhunter C. N., van Moorsel G., Killeen N., Wills K. A., 2001, *MNRAS*, 323, 331
- Morganti R., Sadler E. M., Curran S., 2015, *Advancing Astrophysics with the Square Kilometre Array (AASKA14)*, 134
- Muller S. et al., 2013, *A&A*, 109
- Mundell C. G., Pedlar A., Baum S. A., O’Dea C. P., Gallimore J. F., Brinks E., 1995, *MNRAS*, 272, 355
- Noordermeer E., van der Hulst J. M., Sancisi R., Swaters R. S., van Albada T. S., 2007, *MNRAS*, 376, 1513
- Oliva E., Salvati M., Moorwood A. F. M., Marconi A., 1994, *A&A*, 288, 457
- Orienti M., Morganti R., Dallacasa D., 2006, *A&A*, 457, 531
- Peck A. B., Taylor G. B., Conway J. E., 1999, *ApJ*, 521, 103
- Peck A. B., Taylor G. B., Fassnacht C. D., Readhead A. C. S., Vermeulen R. C., 2000, *ApJ*, 534, 104
- Pihlström Y. M., Vermeulen R. C., Taylor G. B., Conway J. E., 1999, *ApJ*, 525, L13
- Platt J. C., 1999, *Advances in Kernel Methods*, 185
- Prochaska J. X., Herbert-Fort S., Wolfe A. M., 2005, *ApJ*, 635, 123
- Prochaska J. X., Wolfe A. M., 1997, *ApJ*, 487, 73
- Purcell E. M., Field G. B., 1956, *ApJ*, 124, 542
- Rawlings S., Abdalla F. B., Bridle S. L., Blake C. A., Baugh C. M., Greenhill L. J., van der Hulst J. M., 2004, *Science with the Square Kilometer Array*, *New Astronomy Reviews* 48, Carilli C. L., Rawlings S., eds., Elsevier, Amsterdam, pp. 1013–1027

- Reid M. J., Brunthaler A., 2004, *ApJ*, 616, 872
- Roberts M. S., Brown R. L., Brundage W. D., Rots A. H., Haynes M. P., Wolfe A. M., 1976, *AJ*, 81, 293
- Roy N., Chengalur J. N., Srianand R., 2006, *MNRAS*, 365, L1
- Salter C. J., Saikia D. J., Minchin R., Ghosh T., Chandola Y., 2010, *ApJ*, 715, L117
- Srianand R., Gupta N., Momjian E., Vivek M., 2015, *MNRAS*, 451, 917
- Srianand R., Gupta N., Petitjean P., Noterdaeme P., Ledoux C., Salter C. J., Saikia D. J., 2012, *MNRAS*, 421
- Struve C., Conway J. E., 2010, *A&A*, 513, A10
- Taylor G. B., O’Dea C. P., Peck A. B., Koekemoer A. M., 1999, *ApJ*, 512, L27
- Taylor G. B., Peck A. B., Henkel C., Falcke H., Mundell C. G., O’Dea C. P., Baum S. A., Gallimore J. F., 2002, *ApJ*, 574, 88
- Tzanavaris P., Murphy M. T., Webb J. K., Flambaum V. V., Curran S. J., 2007, *MNRAS*, 374, 634
- Urry C. M., Padovani P., 1995, *PASP*, 107, 803
- Uson J. M., Bagri D. S., Cornwell T. J., 1991, *PhRvL*, 67, 3328
- van Gorkom J. H., Knapp G. R., Ekers R. D., Ekers D. D., Laing R. A., Polk K. S., 1989, *AJ*, 97, 708
- van Langevelde H. J., Pihlström Y. M., Conway J. E., Jaffe W., Schilizzi R. T., 2000, *A&A*, 345, L45
- Vermeulen R. C. et al., 2003, *A&A*, 404, 861
- Witten I. H., Frank E., 2011, *Data Mining: Practical Machine Learning Tools and Techniques*. Morgan Kaufmann, San Francisco
- Wolfe A. M., Turnshek D. A., Smith H. E., Cohen R. D., 1986, *ApJS*, 61, 249
- Wopler D. H., 1996, *Neural Computation*, 8, 1341
- Yan T., Stocke J. T., Darling J. K., Momjian E., Sharma S., Kanekar N., 2016, *AJ*, 151, 74
- York B. A., Kanekar N., Ellison S. L., Pettini M., 2007, *MNRAS*, 382, L53
- Zwaan M. A., Liske J., Péroux C., Murphy M. T., Bouché N., Curran S. J., Biggs A. D., 2015, *MNRAS*, 453, 1268